JGR Solid Earth

RESEARCH ARTICLE
10.1029/2020JB019496

Key Points:
- It is a challenge to use sparse sources and receivers deployed in a complex near-surface environment for seismic imaging and monitoring
- It combines surface and buried system by cross correlating direct waves by buried receivers with the reflected waves by surface receivers
- The proposed methods considerably improve seismic repeatability and image quality as demonstrated by 13 seismic surveys

Correspondence to:
Y. Zhao,
zhaoyang@cup.edu.cn

Citation:
Zhao, Y., Niu, F., Liu, H., Jia, X., Yang, J., & Huo, S. (2020). Source-receiver interferometric redatuming using sparse buried receivers to address complex near-surface environments: A case study of seismic imaging quality and time-lapse repeatability. *Journal of Geophysical Research: Solid Earth*, *125*, e2020JB019496. https://doi.org/10.1029/2020JB019496

Received 30 JAN 2020
Accepted 23 APR 2020
Accepted article online 30 APR 2020

Source-Receiver Interferometric Redatuming Using Sparse Buried Receivers to Address Complex Near-Surface Environments: A Case Study of Seismic Imaging Quality and Time-Lapse Repeatability

Yang Zhao[1], Fenglin Niu[2], Hongwei Liu[3], Xueyi Jia[4], Jidong Yang[5], and Shoudong Huo[6]

[1]State Key Laboratory of Petroleum Resources and Prospecting, and Unconventional Petroleum Research Institute, China University of Petroleum (Beijing), Beijing, China, [2]Department of Earth, Environmental and Planetary Sciences, Rice University, Houston, TX, USA, [3]EXPEC Advanced Research Center, Saudi Aramco, Dhahran, Saudi Arabia, [4]Department of Geophysics, Colorado School of Mines, Golden, CO, USA, [5]Department of Geosciences, The University of Texas at Dallas, Richardson, TX, USA, [6]Institute of Geology and Geophysics, Chinese Academy of Sciences, Beijing, China

Abstract Deploying sparse sources and receivers in a complex near-surface environment for seismic imaging and monitoring remains a challenge. Complicated near-surface structures with strong lateral velocity variations and thick weathering layers distort seismic wave paths and produce strong reverberations and scattering. Consequently, acquisition with a buried receiver system below the weathering layer is preferred for land surveys, but the cost of this approach is excessively high in real applications. To mitigate this problem, we propose a source-receiver interferometry-based redatuming method that can generate redatumed data beneath the near surface with a reduced cost. The new acquisition geometry consists of dense surface and sparse buried receivers. The workflow based on source-receiver redatuming combines surface and buried systems by cross correlating direct waves recorded by buried receivers with the corresponding reflected waves recorded by surface receivers. The approach transforms surface source-receiver records into virtually buried source-receiver records. We effectively suppress the acquisition noises associated with the near-surface structures because the proposed technique generates redatumed data below the weathering layer. We apply dip-guided interpolation to the redatumed data to make the geometry consistent with the original surface geometry. The resulting records not only improve the seismic image quality and repeatability compared with the original records but also have a lower cost than a denseburied acquisition system. We use 13 seismic surveys carried out at different times to demonstrate the feasibility and advantage of the proposed method.

1. Introduction

Near-surface imaging and monitoring play an important role in various geophysical applications within the earth. These applications include obtaining engineering information, assessing near-surface structures (faults and channels), and conducting earthquake or deep structure investigations. Nakata and Snieder (2012) applied passive seismic interferometry to a network of strong-motion data sets in Japan to build near-surface velocities, which were then converted into ground soil strength related to the site response to earthquakes. In the area of CO_2 sequestration and storage, fault-bounded structures provide potential pathways for fluids to enter groundwater aquifers. Beilecke et al. (2016) used shear-wave reflections to examine how deeper faults reached near the surface to prevent CO_2 leakage. Bean et al. (2008) demonstrated that inaccurate near-surface models had ubiquitous distortions on earthquake source inversions such as spurious forces and incorrect estimates of moment magnitudes, especially for volcano seismicity associated with large impedance contrasts at the near surface. Göğüş and Pysklywec (2008) confirmed that near-surface observables could be determined for diagnostic expressions of a delaminating or dripping mantle lithosphere.

In the field of exploration geophysics, it is also vital to build an accurate near-surface model for detecting low-relief traps and to increase data quality for recommending well locations (Kelamis et al., 2002). Many

technologies have been used to characterize the complex near surface when the conventional approach was not valid. The complex near surface can include dunes, irregular topography, karst carbonates, and outcropping refractors (Everett, 2012, 2013), which result in strong seismic scattering, free-surface multiples, statics corrections, and source and receiver coupling. Time-lapse seismic monitoring also suffers from seasonal changes and acquisition coupling variations associated with the near surface (Zhao & Li, 2018a). Therefore, redatuming was preferred and developed in recent years since it theoretically bypasses the overburden complexity (Keho & Kelamis, 2012). Model-based redatuming established by Berkhout (1981) and Berryhill (1979) exploited precomputed velocity models to extract redatuming operators. Redatuming was used to mitigate the defocusing effects caused by complex near-surface traits (Yilmaz, 2001). Based on the Kirchhoff or wave-equation extrapolation operators, redatuming introduced such relevant data corrections that sources and receivers were relocated to a certain depth (Schneider et al., 1995). Similar to other conventional techniques, however, the success of model-based redatuming depended on the accuracy of the near-surface velocity model, whereas velocity analysis for complex near surfaces was difficult due to severe statics problems (Bevc, 1997).

Interferometry-based redatuming methods were developed to mitigate the limitations of model-based redatuming (Halliday & Curtis, 2010; Schuster et al., 2004; Schuster & Zhou, 2006). These methods generally required buried receivers to be deployed below the overburden so that the Green's function could be directly measured from the first arrivals. Buried receiver depths depend on the near-surface complexity and vary from meters to a few hundred meters. Interferometry-based methods include daylight imaging (Rickett & Claerbout, 1999), interferometric reflection- or refraction-wave redatuming (Bharadwaj et al., 2012; Mallinson et al., 2011), coda-wave interferometry (Snieder et al., 2002), and virtual-source redatuming (Korneev & Bakulin, 2006). All these methods were based on the weighted cross correlation of different receivers, followed by a summation over all sources or receivers. Specifically, the virtual-source (VS) method was demonstrated to be a powerful redatuming methodology to reduce the complexity of overburden in deep-water environments. The process cross correlated these measured redatuming operators (direct arrivals) with reflected waves to recover the reflection records to image structures below a complex overburden (Bakulin et al., 2007; Bakulin & Mateeva, 2008). Zhao et al. (2019) extended the VS method by constructing a multidimensional radiation-pattern filter in the wavelet domain. This method mitigated the near-surface effects above the buried receivers and mainly improved the time-lapse repeatability for seismic monitoring (Zhao & Li, 2018b). Most of these interferometry-based redatuming methods only involved a single-side cross correlation that brought surface sources to the depth of buried receivers or vice versa. Curtis and Halliday (2010) generalized these predecessors and introduced the theory of source-receiver interferometry, which converted real-source real-receiver pairs into virtual-receiver virtual-source pairs. However, these theorems have yet to be widely adopted in the field due to practical limitations. A dense buried receiver system has not been feasible for large areas due to the high cost, and surface data are insufficient for providing a high-quality image.

One potential way to mitigate this problem is to acquire data using dense surface acquisition and sparse buried receivers. A sparse buried system can significantly reduce the acquisition cost but can record redatuming operators. This proposed geometry combines the advantages of both source-receiver sides and can produce a better image at a lower cost. The seismic repeatability for different surveys is expected to be improved as well since the time-lapse variations are mainly associated with the shallow overburden. To compensate for the sparse geometry of buried receivers at the redatuming level, an effective interpolation technique is critical to make this proposed workflow feasible in practice. Various methods have been developed for seismic interpolations in the geophysical community (Yilmaz, 2001). They use different types of seismic volumes to interpolate data in the gaps to regularize and improve the spatial sampling of the data. One of the popular strategies is to transform the data into a sparse domain and then solve an optimization problem to recover the signal. For example, within narrow-azimuth acquisition, seismic data interpolation was implemented using one-step complex spatial prediction filters (Ronen, 1987) in the frequency-space (FX) domain(Spitz, 1991). Another attractive method is interpolation combined with geologic structures. Structural information was characterized by local dip attributes and was estimated by the energy scanning method (Marfurt, 2006), local structure tensors (Fehmers & Höcker, 2003), and plane-wave destruction (PWD) filters (Fomel, 2002). The quality of interpolation depends on these data attributes. For example, we might choose FX interpolation

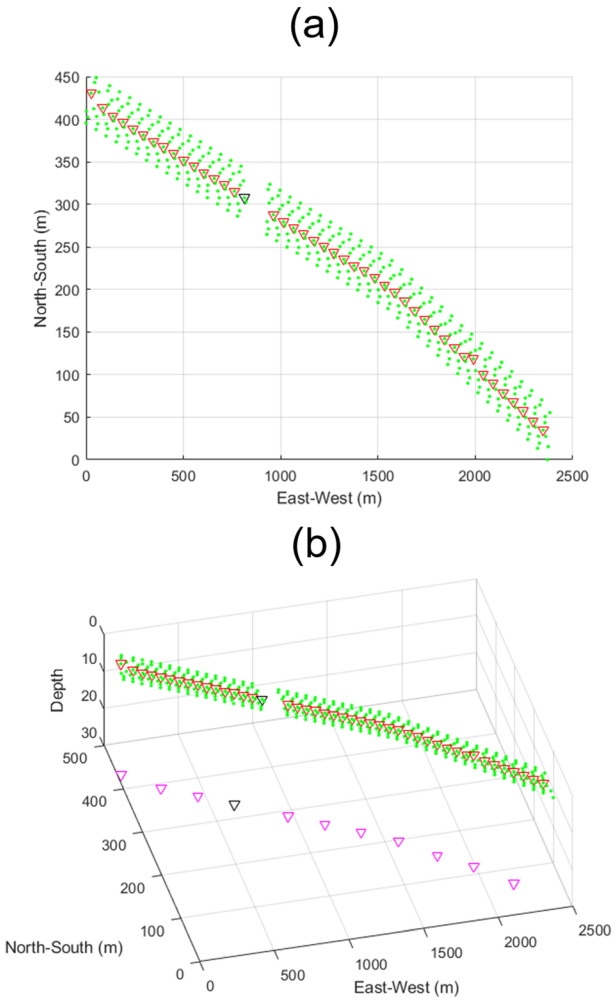

Figure 1. Acquisition geometry for this time-lapse field experiment: nine shot lines consisting of 2,700 surface sources (green asterisks). A line of 300 surface receivers (red triangles) is located at the middle source line. Eighty receiver stations (purple triangles) are buried 30 m below the surface-receiver line. A selected surface receiver and buried receiver is marked in black for illustration. (a) A top-view layout, (b) a half cross-section view.

(Spitz, 1991) if events were aliased in high-frequency areas but not aliased at low-frequency components. In contrast, PWD is a good choice for a simple geological structure.

Based on the same theoretical foundation of source-receiver interferometry (Halliday & Curtis, 2010), we name this proposed technique "source-receiver redatuming." In contrast to these preceding studies, we create a comprehensively innovative workflow to apply the theory to field data. A series of recent land seismic time-lapse surveys from the Middle East with a special acquisition geometry have been selected to evaluate this source-receiver redatuming method. This acquisition consisted of 13 repeated surveys in a desert situation over an oil and gas reservoir. The first survey set (Surveys 1–6) was carried out within 3 months and then the second survey set (Surveys 7¥13) was collected 17 months later. All acquisitions were performed using Mertz 26 vibrators, and most source locations were repeated with a spatial error of less than 1 m. As illustrated in Figure 1, nine shot lines containing 2,700 sources (asterisks in Figure 1) were used for optimum noise removal and effective illumination above the buried receivers. A surface line containing 300 receivers, spaced every 7.5 m, was located in the center of nine shot lines (red open triangles in Figure 1). Another line of 80 buried receivers was placed in vertical boreholes with a spacing of 30 m and a depth of 30 m (purple open triangles in Figure 1b). Figure 2 schematically shows the ray path geometry between the surface sources, receivers, and buried receivers. We sorted seismic records from the common shot domain (records share the same source) to the common receiver domain (records share the same receiver). A common receiver gather from one of the surface receivers in the middle shot line is shown in Figure 3a. In general, the surface records appear to have high-amplitude coda waves caused by near-surface scattering that mask out the targeted deep reflection signals. The thickness of the sand layers varies from 5 to 30 m. The region that is overlain by thick sand has poor seismic data quality. Simple low-dip layers are presented below the complex near surface. Many layers with a great impedance contrast overlie a reservoir reflector at approximately 2,000-m depth (Zhao et al., 2018).

Based on the source-receiver interferometric methodology (Curtis & Halliday, 2010), our proposed work consists of repositioning surface sources and receivers to the depth of sparse buried receivers with an interpolated geometry. We apply dip-guided interpolation to the sparse redatumed data associated with the surface geometry to compensate for the loss of redundancy among surface source-receiver pairs. This enhances the resolution and signal-to-noise ratio (SNR) of the seismic signals when the data are imaged.

1. Sort surface and buried receiver data from the common shot domain into the common receiver domain.
2. Compute direct arrivals from the buried receiver data and estimate redatuming operators for the source and receiver sides.
3. Transform both surface data and direct arrivals into the frequency domain.
4. Perform cross correlations in the frequency domain to redatum surface acquisitions to the locations of buried receivers.
5. Transform redatumed data back into the time domain and interpolate them to the desired geometry.
6. Generate the seismic image volume and examine the image quality and time repeatability.

2. Source Interferometric Redatuming with Sparse Buried Receivers

Seismic interferometry for reflections involves cross correlating the seismic data to the same source recorded at different stations and integrals over all related sources (Bakulin & Calvert, 2006). The geometry of source

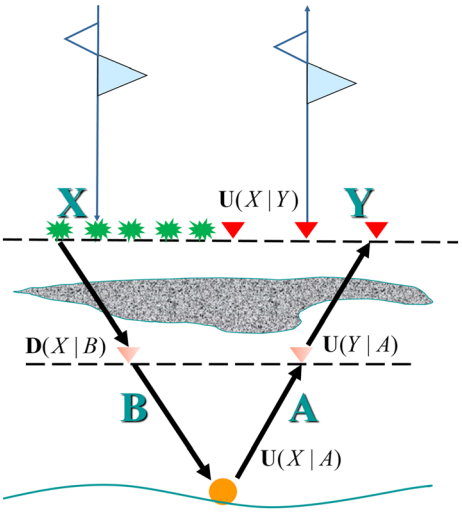

Figure 2. Cartoon illustration of source-receiver interferometric redatuming associated with sparse buried receivers in the presence of heterogeneities near the surface. Surface sources X (green asterisks) generate direct waves $\mathbf{D}(X|B)$ bypassing overburden, recorded by a sparse buried receiver B (light red triangle), which are further reflected by the target (orange circle). The reflection ray path $\mathbf{U}(X|A)$ connects another buried receiver A (light red triangle) with surface receivers Y (red triangles) and results in original surface data sets $\mathbf{U}(X|Y)$. $\mathbf{U}(Y|A)$ are reflected waves from buried receivers to surface receivers displayed in reciprocity form.

interferometric redatuming is illustrated in Figure 4. An elastic derivation of the interferometry theorem is preferred, which requires adequate separation of P- and S-wave components (Wapenaar, 2004; Wapenaar et al., 2011). However, we only work with the vertical component (P-wave) due to the shortage of multicomponent recordings. Therefore, these elastic situations are approximated by acoustic formulations based on the acoustic representation theorem (Curtis & Halliday, 2010; Halliday & Curtis, 2010; Ramírez & Weglein, 2009; Wapenaar, 2004) in the frequency domain (Dong et al., 2009; Schuster et al., 2004) as

$$V(B|Y;\omega) - V^*(B|Y;\omega) \approx \int_{surface} \left[D^*(X|B;\omega)\frac{\partial U(X|Y;\omega)}{\partial n_X} - U(X|Y;\omega)\frac{\partial D^*(X|B;\omega)}{\partial n_X} \right] d^2X, \quad (1)$$

where the superscripts * and ω denote the complex conjugate and angular frequency, respectively. Y and B denote the spatial coordinates of the dense surface and sparse buried receivers, respectively, and X represents the source location (Figure 4). $V(B|Y;\omega)$ is the interferometric Green's function at the surface receiver Y when the buried receiver B is treated as a virtual source. The direct arrival $D(X|B;\omega)$ is excited by the surface source X and recorded by the buried receiver B, while the reflected wavefield $U(X|Y;\omega)$ is excited by the same source X but is recorded by the surface receiver Y. n_X represents the normal direction of the integration surface. The far-field approximated representation of equation 1 yields

$$V(B|Y;\omega) - V^*(B|Y;\omega) \approx 2i\frac{\omega}{c}\int_{surface} D^*(X|B;\omega)U(X|Y;\omega)d^2X. \quad (2)$$

A detailed derivation of equation 2 can be found in Van Der Neut et al. (2015). c is the sound speed at the surface. Figure 3b illustrates a common receiver gather ($U(X|A) \rightarrow U(A|X)$) recorded at a selected buried geophone (black triangle in Figure 1b). Buried receivers B yield deep reflections with much higher SNR than surface seismic data Y. The original near-offset arrivals are considered direct wavefields (offset <30 m and time < 100 ms). The values of the offset and time are assessed based on the fact that these early waves are mainly occupied by direct P-waves. These reflections (time > 300 ms) from all offsets are considered reflected waves.

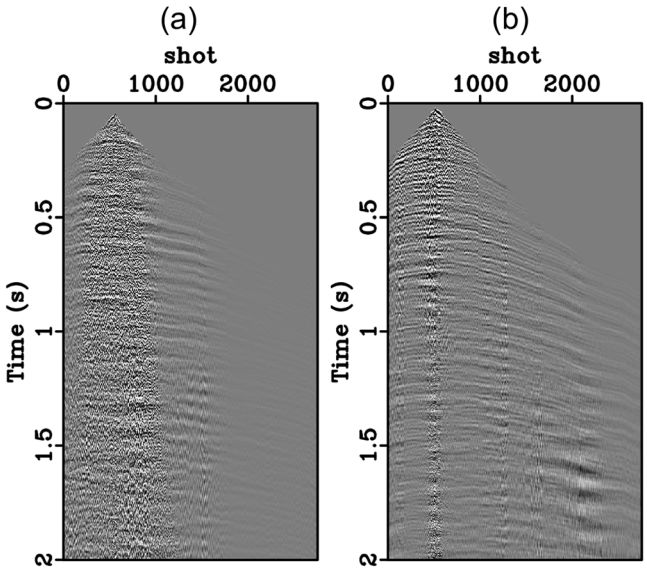

Figure 3. Two examples of common receiver gathers at two selected receivers (black triangles in Figure 1), which consist of 2,700 shots after noise removal. (a) A surface receiver record suffers a low SNR. (b) A buried receiver record yields a much higher SNR than (a).

Source interferometric redatuming converts buried receivers into virtual sources V by summing the available surface sources inside the stationary-phase zone (Snieder et al., 2002). However, the redatumed data still suffer from near-surface complexity, as the surface receivers Y have not yet been corrected for depth. The loss of data redundancy may also result in severe degradation due to the sparseness of B. To address these issues, we need to perform another round of cross correlations for receiver redatuming and increase data redundancy.

3. Source-Receiver Interferometric Redatuming

To perform complete source-receiver redatuming effectively, we need to regroup $V(B|Y)$ from a common shot domain to a common receiver domain $V(Y|B)$ so that the buried receivers B and the surface receivers Y can switch geometrically according to the seismic reciprocity principle. Figure 5 summarizes this redatuming process, which can be formularized similarly to equation 2:

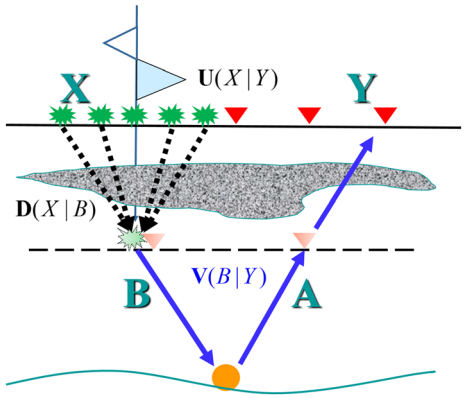

Figure 4. Cartoon illustration of the source-side redatuming stage in the source-receiver redatuming. Surface data $\mathbf{U}(X|\,Y)$ are cross correlated with direct waves $\mathbf{D}(X|\,B)$ (black dashed lines) recorded at buried receiver B (light red triangle) and summed over available sources to produce the buried virtual source (light green asterisk) and source-side redatuming data $\mathbf{V}(B|\,Y)$ (blue arrows). The available shots are surface sources located inside the stationary phase zone for buried receiver B.

$$V(A|B;\omega) - V^*(A|B;\omega) \approx 2i\frac{\omega}{c}\int_{buried} D^*(Y|A;\omega)V(Y|B;\omega)d^2Y. \quad (3)$$

Here, $V(A|\,B;\omega)$ are the resulting redatumed data at the buried receiver B when the buried receiver A is treated as a virtual source (Figure 5). Direct arrivals $D(Y|\,A;\omega)$ are supposed to be generated from surface receivers Y recorded by the buried receivers A, whereas the system only has sources X rather than Y. This results in an acquisition drawback that requires sources X located close to receivers Y. As shown in Figure 1, we can take advantage of the fifth shot line located next to the surface receiver line. The average source-receiver distance is less than 5 m. Figure 6a provides a 2-D cartoon section on how we approximate $D(Y|\,A)$ to $D\left(\widehat{X}|A\right)$, where X represents the nearest shot and has an equivalent number Y. A common receiver gather sorted by the offset of the original direct waves $D(X|\,A)$ is shown in Figure 6b, which shows large variations in the waveform of the direct P-wave, indicative of near-surface complexity. We find that the direct P amplitude recorded at the buried receiver A varies systematically with respect to X in terms of different angles. The small-angle traces present large amplitudes, whereas large angles are relatively small since A is the vertical component record. With this approximation, substituting equation 2 into equation 3 results in

$$\begin{aligned} V(\mathrm{A\ B};\omega) - \mathrm{V}^*(\mathrm{A\ B};\omega) \approx -4\left(\frac{\omega}{c}\right)^2 \int_{buried} D^*(\mathrm{Y\ A};\omega) \\ \left\{\int_{surface} U(\mathrm{Y}|X;\omega)\mathrm{D}^*(\mathrm{B}|X;\omega)\mathrm{d}^2X + V^*(\mathrm{B}|Y;\omega)\right\}d^2Y \\ V(\mathrm{A\ B};\omega) - \mathrm{V}^*(A\ B;\omega) \approx -4\left(\frac{\omega}{c}\right)^2 \int_{surface}\int_{buried} D^*(\mathrm{Y\ A};\omega)\mathrm{U}(\mathrm{Y}|X;\omega)\mathrm{D}^*(\mathrm{B}|X;\omega)\mathrm{d}^2Xd^2Y \\ -4\left(\frac{\omega}{c}\right)^2 \int_{surface} D^*(\mathrm{Y}|A;\omega)\mathrm{V}^*(\mathrm{B}|Y;\omega)\mathrm{d}^2Y, \end{aligned} \quad (4)$$

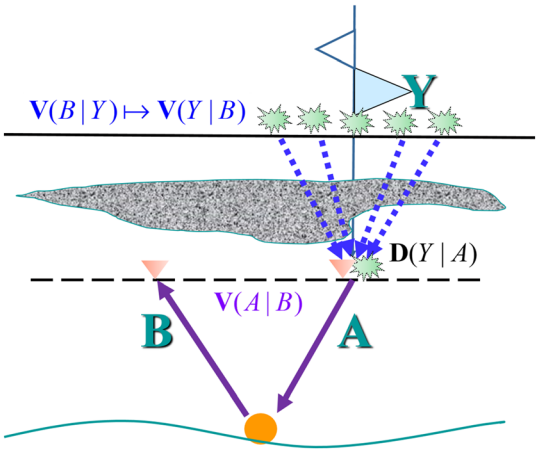

Figure 5. The receiver-side redatuming stage in the source-receiver redatuming. $\mathbf{V}(B|\,Y)$ regroup into $\mathbf{V}(Y|\,B)$ by switching the source and receiver dimensions according to seismic reciprocity. The new $\mathbf{V}(Y|\,B)$ are then cross correlated with direct waves $\mathbf{D}(Y|\,A)$ (blue dashed arrows) recorded at buried receiver A (light red triangle) and summed over available shots to produce another virtual source (light green asterisk) and the source-receiver redatuming data $\mathbf{V}(A|\,B)$ (purple arrows).

where the last integral of the right-hand side is the anticausal term corresponding to the redatumed data $-V^*(A|B;\omega)$. We only use the causal part of the redatumed data, and after inserting $D\left(\widehat{X}|A\right)$ into $U(Y|\,X)$, equation 4 can be simplified as

$$V(A|B;\omega) \approx -4\left(\frac{\omega}{c}\right)^2 \int_{surface}\int_{buried} D^*\left(\widehat{X}|A\right)U(Y|X;\omega)D^*(B|X;\omega)d^2Xd^2Y. \quad (5)$$

Equation 5 indicates that source-receiver redatuming can be computed by cross correlating the original surface data with the direct P-waves recorded at the buried receivers in the common receiver domain. Note that equation 4 and its simplified version, equation 5, can be found in many works (e.g., Berkhout, 1981; Berryhill, 1979). However, most of these studies employed model-driven redatuming with the operators D calculated from a velocity model instead of data, except for Curtis and Halliday (2010), who also derived these two equations for data-driven interferometric redatuming based on the representation theorem. In this study, we construct comprehensive data-driven workflows and validate them with field data sets. As illustrated in Figure 7a, the resultant gather with data calculated from equation 5 yields a higher SNR than that in

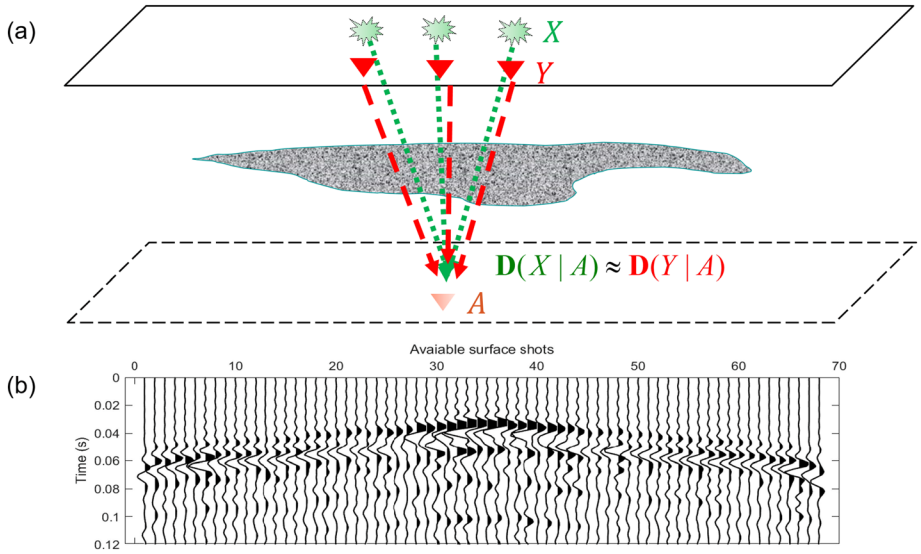

Figure 6. (a) Cartoon illustration of the approximated direct waves in receiver-side redatuming (Figure 5). The nearby sources X (green asterisks) are used to approximate surface receivers Y(red triangles): $\mathbf{D}(X|A) \approx \mathbf{D}(Y|A)$. The average distance between X and Y is less than 5 meters. (b) the common receiver gather $\mathbf{D}(X|A)$ of direct waves of the selected buried receiver A (the light red triangle in (a)) sorted by the offset. The available shots are surface sources located inside the stationary phase zone for A.

Figure 3a, especially for shallow reflectors due to dampened near-surface scattering. Note that the amplitude spectrum of $U(Y|X)$ is multiplied by redatuming operators twice in the frequency domain. Therefore, the final $V(A|B)$ has an inaccurate spectrum compared with the original surface data sets. If we want to make a fair comparison with nonredatuming data sets for time-lapse purposes, we need to apply a zero-phase whitening filter H(Weemstra et al., 2014) to $D\left(\widehat{X}|A\right)$ and $D(B|X)$ to maintain the original spectrum as $U(Y|X)$. Plugging H into equation 4 produces the final redatuming result as

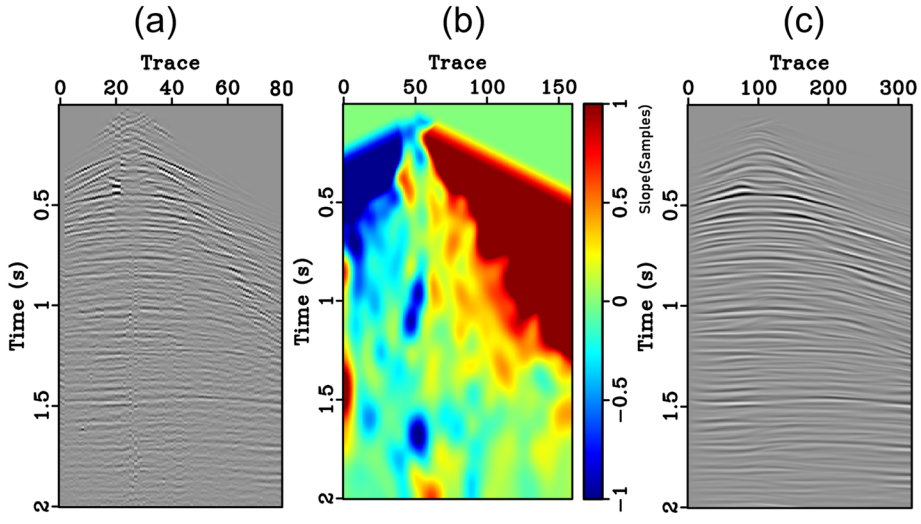

Figure 7. A dip-guided PWD interpolation process of the selected buried receiver (black triangle in Figure 1): (a) source-receiver redatuming data $\mathbf{V}_H(A|B)$ (80 traces, 30-m spacing) before interpolation; (b) expanded dip estimation using the proposed PWD operator; (c) after interpolations $\tilde{\mathbf{V}}_H(A|B)$ (320 traces, 7.5-m spacing). An improved resolution and smoothing effect are observed from (a) to (c).

$$V_H(A|B;\omega) \approx -4\left(\frac{\omega}{c}\right)^2 \int_{surface} \int_{buried} \left[HD\left(\widehat{X}|A;\omega\right)\right]^* U(Y|X;\omega)[HD(B|X;\omega)]^* d^2X d^2Y. \quad (6)$$

$V_H(A|B)$ is an 80×80 redatumed data profile with dimensions of the number of buried receivers, originating from $2{,}700 \times 300$ in this example. Figure 7a suggests a significant drop in data redundancy after a summation of surface X and Y; therefore, interpolation should be applied to $V_H(A|B)$ to make it comparable to the surface $U(Y|X)$.

4. Dip-Guided Interpolation at the Redatuming Depth

It is well-known that most seismic interpolations are easy to implement when using simple, linear and stationary seismic data sets (Ronen, 1987). The interpolation can be applied before redatuming, but we choose to apply the interpolation after equation 4 because the redatumed records can reduce the overburdened complexities as the sources and receivers are virtually placed below the near surface. Recall the specific geology settings of this field data discussed in the introduction section: below the complex overburden are simple layer-cake structures with dip angles less than 4°. A $V_H(A|B;\omega)$ containing flat reflectors with a mild lateral variation is well suited to the dip-guided interpolation method based on plane-wave prediction filters (Fomel, 2010; Xue et al., 2019).

Plane-wave destruction (PWD) is a method used to evaluate the dip of seismic records. It predicts the next seismic trace by phase shifting the previous trace along the dominant event slope while maintaining the trace amplitude. The estimated dominant slope is then calculated by minimizing the prediction error (Fomel, 2010). Shape regularization constrains the estimated dips to vary smoothly for the redatumed data. Because PWD is usually employed in the time domain, we first transform $V_H(A|B;\omega)$ to the time domain:

$$V_H(A|B;\, t) = F_{\omega \to t}\{V_H(A|B;\omega)\}, \quad (7)$$

where $F_{\omega \to t}$ denotes the Fourier transform. We simplify the notation by using V_H and formularize the interpolation as a regularized classic least-squares goal $V_H P \approx \delta$ or

$$\begin{bmatrix} 1 & & & & \\ V_2 & V_1 & & & \\ V_3 & & V_2 & & \\ \cdots & & & \cdots & \\ V_n & & & & V_{n-1} \end{bmatrix} \begin{bmatrix} 1 \\ -P_{2,1} \\ -P_{3,2} \\ \cdots \\ -P_{n,n-1} \end{bmatrix} \approx \begin{bmatrix} 1 \\ 0 \\ 0 \\ \cdots \\ 0 \end{bmatrix}, \quad (8)$$

where $P_{n,n-1}$ is the dip field between traces n and $n-1$, which is associated with the PWD operator. V_n is the nth trace of the redatumed data. Equation 8 is not a Yule-Walker equation since we only use adjacent traces rather than a prediction filter H within a certain length. This approximated equality implies that the solution can be obtained by solving a least square problem, such as $P \approx (V_H{}^T V_H)^{-1} V_H{}^T \delta$, mathematically:

$$\begin{bmatrix} -P_{1,0} \\ -P_{2,1} \\ -P_{3,2} \\ \cdots \\ -P_{n,n-1} \end{bmatrix} \approx \begin{bmatrix} \sum_{i=2}^{n} V_i^2 & & & & \\ & V_1^2 & & & \\ & & V_2^2 & & \\ & & & \cdots & \\ & & & & V_{n-1}^2 \end{bmatrix}^{-1} \begin{bmatrix} 1 & V_2 & V_3 & \cdots & V_n \\ & V_1 & & & \\ & & V_2 & & \\ & & & \cdots & \\ & & & & V_{n-1} \end{bmatrix} \begin{bmatrix} 1 \\ 0 \\ 0 \\ \cdots \\ 0 \end{bmatrix}, \quad (9)$$

where we can directly solve equation 9 to obtain the dip field P since the inverse of a diagonal matrix is very easy to solve. Figure 7b shows the calculated dip from the input data, and it has been smoothed to make an extended dip field $\tilde{P}$ that has the same length $\tilde{n}$ as the target interpolated redatumed data $\tilde{V}_H$. One alternative to reconstruct $\tilde{V}_H$ is to solve a linear system with the inverse PWD as a linear operator. The linear problem is the switching matrix position in equation 9 as $\tilde{P}\tilde{V}_H \approx \delta$ or

$$\begin{bmatrix} I & & & & & & & \\ -P_{2,1} & I & & & & & & \\ & -P_{3,2} & I & & & & & \\ & & -P_{4,3} & I & & & & \\ & & & \cdots & \cdots & & & \\ & & & & & \cdots & & \\ & & & & & & -P_{\tilde{n},\tilde{n}} & \end{bmatrix} -1I \begin{bmatrix} & & & & \cdots & \\ \tilde{V}_1 & \tilde{V}_2 & \tilde{V}_3 & \cdots & \cdots & \tilde{n} \\ & & & & & \tilde{V} \end{bmatrix} \approx \tilde{V}_1 \begin{bmatrix} 1 \\ 0 \\ 0 \\ \cdots \\ \cdots \\ \cdots \\ 0 \end{bmatrix}. \tag{10}$$

This linear problem can be solved efficiently by $\tilde{V}_H \approx \left(\tilde{P}^T \tilde{P}\right)^{-1} \tilde{P}^T \delta$. Interpolation with a structural constraint can also be carried out, and the interpolated redatumed data are

$$\begin{bmatrix} \widetilde{V}_1 \\ \widetilde{V}_2 \\ \widetilde{V}_3 \\ \cdots \\ \cdots \\ \cdots \\ \widetilde{V}_{\tilde{n}} \end{bmatrix} \approx \begin{bmatrix} I + \left(P_{2,1}\right)^2 & -P_{2,1}I & & & & & & \\ -P_{2,1}I & I + \left(P_{3,2}\right)^2 & -P_{3,2}I & & & & & \\ & -P_{3,2}I & I + \left(P_{4,3}\right)^2 & & & & & \\ & & & \cdots & \cdots & & & \\ & & & & & \cdots & -P_{\tilde{\tilde{n}},\tilde{n}-1}I & \\ & & & & & -P_{\tilde{\tilde{n}},\tilde{n}-1}I & I + \left(P_{\tilde{n}} + 1, \widetilde{n}\right)^2 & \end{bmatrix}^{-1} \begin{bmatrix} I & -P_{2,1} & & & & & \\ & I & -P_{3,2} & & & & \\ & & I & -P_{4,3} & & & \\ & & & \cdots & & & \\ & & & \cdots & \cdots & & \\ & & & & & \cdots & \\ & & & & & -P_{\tilde{\tilde{n}},\tilde{n}-1} & I \end{bmatrix} \begin{bmatrix} \widetilde{V}_1 \\ 0 \\ 0 \\ \cdots \\ \cdots \\ \cdots \\ 0 \end{bmatrix}. \tag{11}$$

Equation 11 is a typical band diagonal matrix and can be solved efficiently with conjugate gradients (Hestenes & Stiefel, 1952). Alternatively, equations 9 and 11 can be solved iteratively. The interpolated gather $\tilde{V}_H$ shows a better SNR and enhanced resolution while preserving the slope, as shown in Figure 7c.

Comparing Figure 7c with Figure 7a, we observe strong smoothing effects from plane-wave destruction due to the smoothing regularization in this filter. It is important to distinguish these side effects from redatuming to mitigate their influence. A classic synthetic image from Claerbout and Fomel (2006) is selected to examine our derived PWD algorithm. This classic image contains dipping beds, an unconformity and a fault. Figure 8a shows the subsampled version (one-fourth sampling rate), and we want to recover the original image from this image. Figure 8b shows the dip estimated from the input image, and it has been smoothed similarly to generate a dip that has the same dimension as the target image. By solving equation 11, we can obtain the interpolation result, as shown in Figure 8c. Figure 8d shows its difference from the true reference image. The interpolated results act as a smoother version of the inputs, and residuals only around the unconformity and fault can be observed. Figure 8 validates that the influences from our PWD interpolation are controllable for this study.

5. Image Quality and Repeatability

Thirteen time-lapse seismic surveys were performed before CO_2 sequestration activities over an oil reservoir. Two data sets were acquired using a 2-D line of 300 surface receivers (7.5-m spacing) and 80 shallow buried

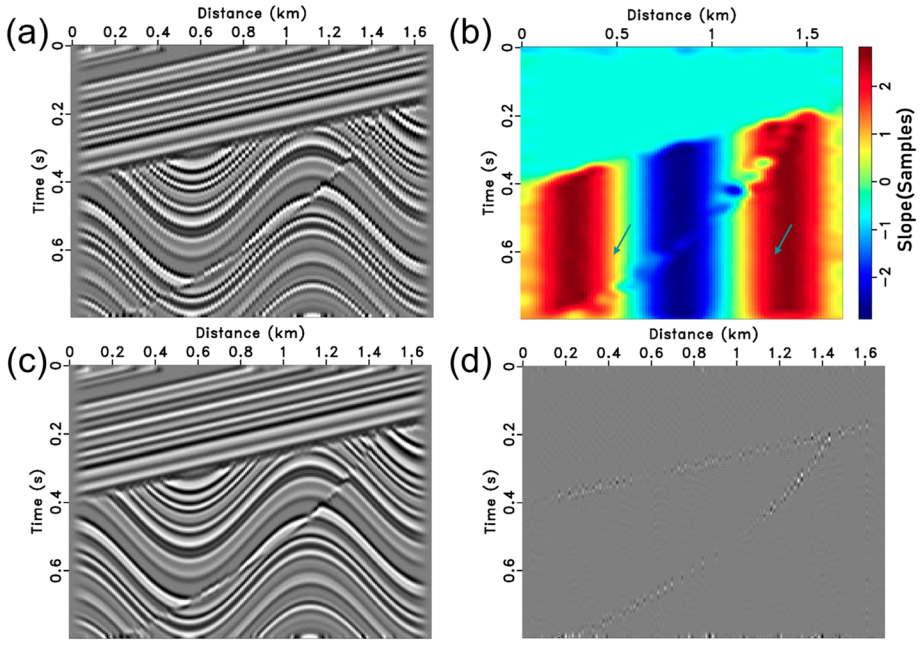

Figure 8. A classic synthetic image for the dip-guided PWD interpolation process. (a) Synthetic input image containing steep structures and a fault (56 traces, 30-m spacing); (b) dip estimation using the proposed PWD operator; (c) interpolation result (224 traces, 7.5-m spacing); (d) difference compared to the true reference image. In addition to an improved resolution and SNR, residuals only around the unconformity and fault can be found.

receivers (30-m spacing). Surface source (7.5-m spacing) equipment with vibroseis was repeatedly used over 19 months. The maximum offset was 2,400 m. This acquisition design was expected to take advantage of combining surface and receiver systems to correct positioning errors, coupling variations, and diurnal/seasonal changes in seismic 4-D processing. Bakulin et al. (2014) suggested that the repeatability and image quality of data from surface receivers are heavily influenced by shallow near-surface factors such as poor illumination beneath the thick sand layer and significant shifts between the first survey set (Surveys 1–6) and the second survey set (Surveys 7–13).

To assess the performance gain and implement a comparison with existing techniques, the same workflow of the field surveys is performed in three stages. The three stages are surface-wave noise removal, source-receiver interferometric redatuming, and gather stacking. The first stage contains a summation of nine source lines to reduce bursts from the large-amplitude traces, random energies, and scattered noises. To take advantage of the dense source spacing, these common shot domain gathers are then arranged into common receiver gathers, and an FK filter is applied to mitigate surface-wave noise. Figure 3 illustrates the first stage results for surface and buried receivers, respectively. In the second stage, the proposed source-receiver redatuming is evaluated. An autopicking algorithm (Zhang et al., 2003) is performed to select the direct waves within a 60-ms window (Figure 3b) to serve as the redatumed operators $D\left(\widehat{X}|A\right)$ and $D(B|X)$. The second stage bypasses the overburden by sinking the surface acquisition using two interferometric cross correlations. In the third stage, an amplitude gain is performed on the individual receiver for every five discrete 500-ms windows. Gather stacking contains the arithmetic sum for all resulting interferometric gathers and recovery scaling to balance energy. Gather stacks of two traditional nonredatuming methods using surface $U(Y|X)$ and buried $U(A|X)$ are generated in comparison with the exact flow without the second stage. The entire workflow is summarized in Figure 9.

We plot the three resulting images of $U(Y|X)$, $U(A|X)$, and $\tilde{V}_H(A|B)$ from Survey 1 in Figure 10. A selected shallow reflector of the target reservoir is highlighted by green and blue arrows. The surface receiver section (Figure 10a) has the worst SNR in terms of the target reservoir. The right-hand side of the shallow reflector has extremely poor illumination beneath the thick sand. The buried receiver section (Figure 10b) shows less

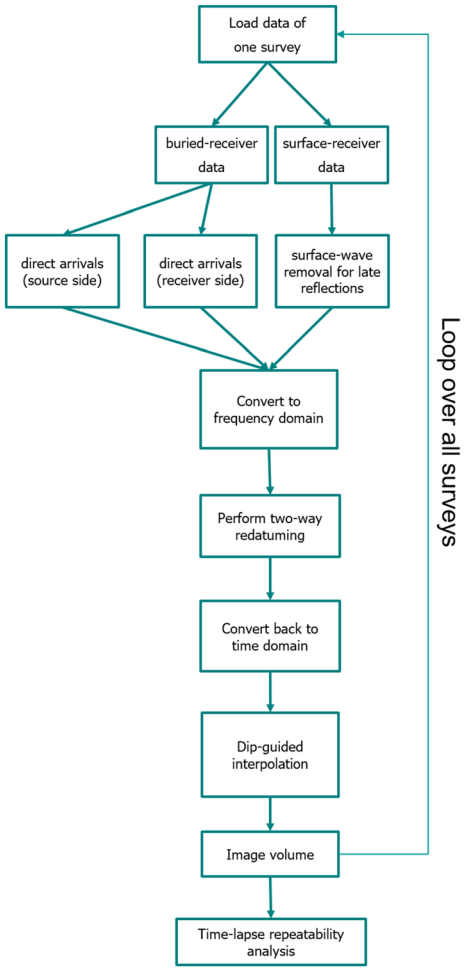

Figure 9. The summarized workflow is colored in green for the proposed method. The input data are both from the buried and receiver receivers, and the output comprises the time-lapse seismic image volume with the proposed technique. A more detailed description is provided in the main text.

noise with more continuous reflections in the target zone than the surface receiver section. Specifically, the buried receivers show significantly improved illumination for the marked shallow reflector beneath the thick sand layer even without redatuming. Finally, the source-receiver redatuming section (Figure 10c) has the best SNR and illumination. The shallow reflector shows balanced illumination in which the thickness of the near-surface sand layer has completely resolved, while the target reflector becomes more continuous. These observations demonstrate the robustness of the source-receiver redatuming workflow, and these resulting images can serve as better inputs for velocity analysis and migration.

In addition to image quality, repeatability is another important factor in measuring the quality of seismic monitoring. Figure 11 shows a comparison using one trace from the 13 surveys to assess the outcome of each technique on repeatability. A strong repeatability issue of the surface receiver section is observed between the first survey set (Surveys 1–6) and the second survey set (Survey 7–13, Figure 11a), especially for the target reservoir and the selected shallow reflector. This subject is described by a gap in the waveform between Surveys 6 and 7, which is caused by a 1-year gap in acquisition. Figure 11b shows better repeatability for both reflectors compared with Section a. It is straightforward to see that the buried receiver section partially reduces the near-surface vacations from the receiver side, but a reduced discontinuity between Surveys 6 and 7 still exists since the source side is not redatumed to the buried depth. Figure 11c shows the result after applying the proposed processing workflow, which virtually places both the surface sources and the buried receivers at the depth of the latter. Markedly upgraded repeatability appears across this survey gap, resulting in the best repeatability.

The normalized root mean square (NRMS) over a small window around the target reservoir is selected to measure the repeatability (Kragh & Christie, 2002). The NRMS is expressed as a percentage that is measured between two seismic sections in a given window and divided by their average RMS. The NRMS is designed to be extremely sensitive to the finest variations in seismic activity. The NRMS is calculated between different combinations of all 13 surveys. This results in 78 NRMS values at each trace. The NRMS histogram for each technique is shown in Figure 12. The surface receiver section (red line) indicates a bimodal NRMS distribution with two separated peaks of approximately 35% and 100%. As expected, the greater NRMS values are from the gap between the first survey set (Survey 1–6) and the second survey set (Survey 7–13). The two separated peaks have a different shape, which suggests significant nonrepeatability for surface receiver data. A narrower and less pronounced distribution (peaks of approximately 20% and 70%) than the surface receiver section is observed for the buried receiver section. However, the 1-year gap still exists since we have not virtually buried the sources at depth yet. The source-receiver redatuming method closes this gap and produces a single-mode distribution with the best NRMS values positioned at 32% (black). These outcomes support the remarks from Figure 11. This indicates that the proposed strategy can successfully mitigate near-surface impacts between surveys separated by a 17-month gap and, more importantly, result in significantly higher image quality than the conventional VS method.

6. Discussion

Although this study is mainly focused on petroleum exploration geophysics, it can be readily expanded to other applications within the scope of solid earth geophysics. For instance, our proposed strategy may be directly implemented as a time-lapse mode to image changes in subsurface fluid flow over time due to

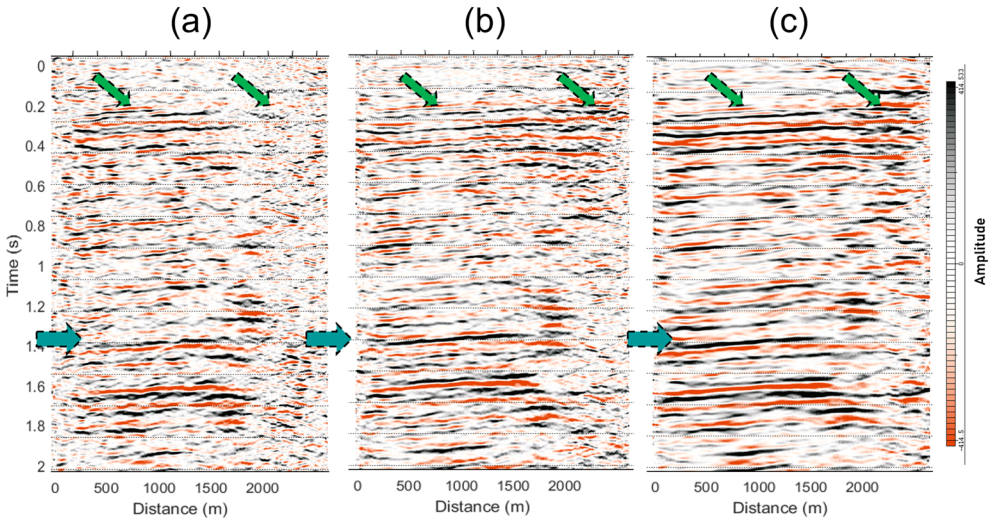

Figure 10. Seismic images obtained from (a) nonredatumed surface data, (b) nonredatumed buried data, and (c) source-receiver redatumed data. The target reservoir reflector (blue arrows) and selected shallow reflectors (green arrows) demonstrate the SNR improvement from (a) to (c). Panel (c) has the best continuity and resolution of all three sections, which demonstrates the robustness of the proposed source-receiver redatuming workflow.

CO_2 sequestration projects, groundwater flow, or environmental contaminant remediation (Beilecke et al., 2016). Source-receiver interferometric redatuming has been demonstrated to reduce overburden complexity by a series of field experiments; therefore, the proposed method may be adapted to investigations of deep structure if earthquakes are recorded at a complex near-surface site (Bean et al., 2008). On the other hand, the recorded direct arrivals at sparse buried receivers contain valuable information for near-surface characterization. Classic methods such as transmission wave tomography may be applied to interpolated redatuming operators to reconstruct high-resolution profiles that are very useful for civil engineering, site characterization, and disaster prevention.

We can also apply conventional virtual source redatuming to field data such that the surface sources are virtually placed at the buried receivers. Comparing the results with the proposed method, the major advantage

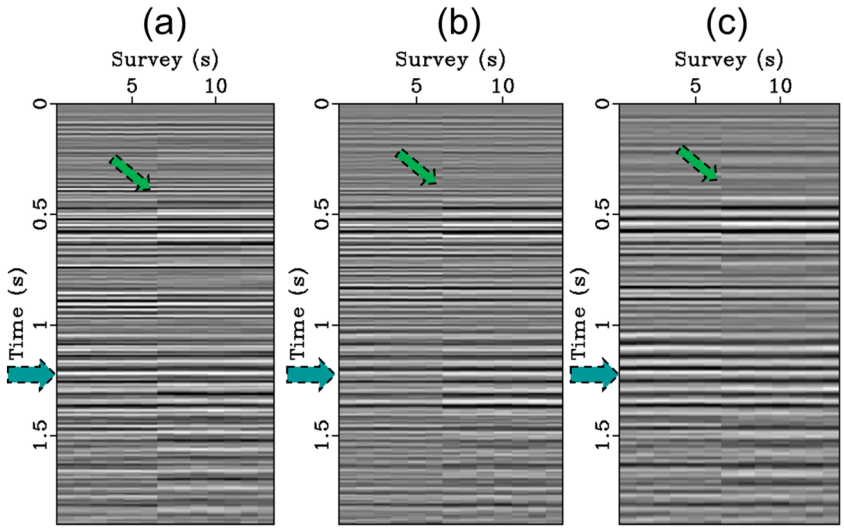

Figure 11. One trace for all 13 surveys including results from (a) nonredatumed surface data, (b) nonredatumed buried data, and (c) source-receiver redatumed data. Similar to Figure 10, the same target reservoir reflector (blue arrows) and shallow reflectors (green arrows) demonstrate the repeatability improvement from (a) to (c). Panel (c) has the best repeatability and demonstrates the robustness of the proposed source-receiver redatuming workflow again.

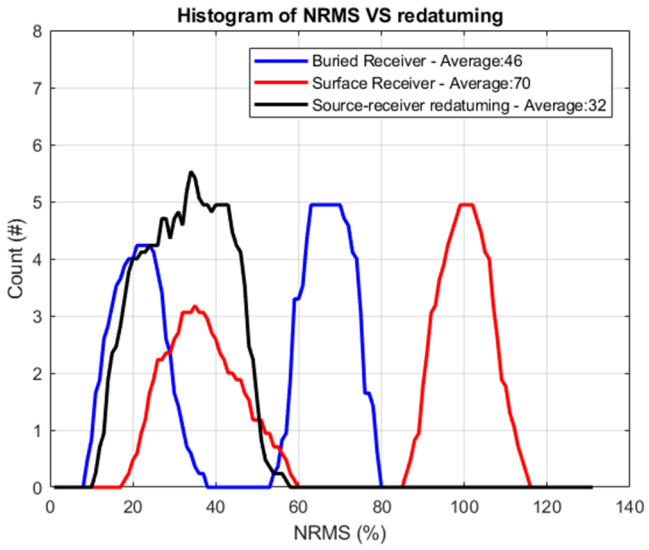

Figure 12. Histogram showing the NRMS values computed using the three processing flows from the field-data example (Figure 11). Median values of each distribution are displayed in the legend. The proposed source-receiver redatuming produces a single-mode distribution with the best NRMS of 32% (black line). This quantitatively validates the observations from Figure 11.

of source-receiver redatuming is a considerably improved image quality, as a large number of surface receivers are used. However, the repeatability obtained from source-receiver redatuming is slightly worse than that of conventional virtual source redatuming. One possible explanation is that interferometric redatuming is not intended to remove all the near-surface influence. A complete deconvolution of downward and upward wavefields is essential when wavefield separations are available (Wapenaar et al., 2011). Redatuming surface receivers to depth is a double-edged sword, and therefore, the tradeoff between image quality and repeatability needs to be carefully assessed.

Another drawback of the proposed method is the requirement for the surface acquisition geometry. A line of sources needs to be placed close enough to the surface receiver so that we can directly measure the receiver-side redatuming operator. Indirect measurements, such as long-offset refraction waves, often return a lower SNR for approximating these redatuming operators. Modern land acquisition easily satisfies this requirement without extra cost.

We use dip-guided interpolation, which is suitable for the relatively simple structure below the near surface. Other interpolation methods, such as FX interpolation, can also be used. The interpolation operator is solved by a set of a linear systems whose coefficients are based on the spectrum of the spatial prediction filter determined by the recorded traces. The periodicity at low frequency may be used to predict the shape of the higher-frequency components and therefore can guide the interpolation of events that are aliased at high frequencies. Low-frequency components are less affected by the near surface due to their long wavelength. We apply FX interpolation to this data set and produce similar results for imaging quality and repeatability. As demonstrated in Figures 7 and 8, it is evident that the image improvements are partially attributable to PWD interpolation because of its smoothing effects, whereas the time-lapse repeatability is not affected by PWD. We are currently in a preliminary interpolation selection stage, in which the approach is determined in a heuristic way instead of through systematic optimization. A more robust and adaptive approach to source-receiver redatuming is one of our ongoing research directions.

Strictly speaking, an elastic theme of interferometric redatuming is preferred and requires sufficient P- and S-mode separations (Curtis & Halliday, 2010). Given the absence of multicomponent records, we assess this land environment by acoustic derivations. The elastic derivations should be adapted to future applications when horizontal components are available. Similar to interferometric redatuming methods, we want to emphasize that this method is only able to reduce the contamination induced by the near surface but cannot eliminate all the overburden effects.

7. Conclusions

To mitigate geophysical issues related to complex near-surface environments and to reduce the cost of densely buried acquisition, we propose a data-driven workflow using both surface and buried receivers based on source-receiver interferometry. This specific geometry consists of dense surface sources, surface receivers, and sparse buried receivers. The sparseness of the buried system effectively reduces the acquisition cost but is still able to record the direct arrivals containing near-surface information. These direct arrivals are processed as redatuming operators for the source and receiver sides and then the source-receiver cross correlates with the surface reflection data to virtually place sources and receivers at sparse buried locations. We apply dip-guided structure interpolation to make the geometry of the redatumed data consistent with the surface geometry. The source-receiver redatuming workflow can handle complex near surfaces with strong lateral velocity variations. We achieve better image quality and repeatability of the reservoir target because redatumed sources and receivers are closer to the target, and the scattering noises associated with the near surface are suppressed. Compared to other existing redatuming methods, the proposed procedure is independent of the velocity model and has a lower acquisition cost. Moreover, the process does not

require extensive human intervention, providing an automated processing workflow for high-quality imaging. As time-lapse noise is mainly caused by near-surface variations, the method can improve time-lapse repeatability and imaging quality by reducing near-surface influences on reflection signals. We demonstrate these improvements using 13 time-lapse surveys that prominently reduce a significant repeatability problem across a 17-month survey gap. Source-receiver redatuming is a positive step forward for land seismic monitoring.

Acknowledgments
We would like to thank Saudi Aramco for providing us with the waveform data and for giving us permission to publish the results. We specifically express our appreciation to Cristina Young for her critical work on improving this paper. We would like to thank the Editor, Prof. Michael Bostock, the Associate Editor, Prof. Sebastien Chevrot, and two anonymous reviewers for their comments and suggestions, which significantly improved the quality of this paper. This study is jointly supported by the National Key R&D Program of China (2017YFC1500303) and the Science Foundation of China University of Petroleum, Beijing (2462019YJRC007). The associated data and codes used by this paper are available at the following link with the DOI from Zenodo: DOI: https://doi.org/10.5281/zenodo.3539287

References

Bakulin, A., & Calvert, R. (2006). The virtual source method: Theory and case study. *Geophysics*, *71*(4), SI139–SI150. https://doi.org/10.1190/1.2216190

Bakulin, A., & Mateeva, A. (2008). Estimating interval shear-wave splitting from multicomponent virtual shear check shots. *Geophysics*, *73*(5), A39–A43.

Bakulin, A., Mateeva, A., Mehta, K., Jorgensen, P., Ferrandis, J., Herhold, I. S., & Lopez, J. (2007). Virtual source applications to imaging and reservoir monitoring. *The Leading Edge*, *26*(6), 732–740.

Bakulin, A., Smith, R., Jervis, M., & Burnstad, R. (2014). Near surface changes and 4D seismic repeatability in desert environment: From days to years. In *84th Annual International Meeting, SEG, Expanded Abstracts* (pp. 4843–4847). https://doi.org/10.1190/segam2014-0429.1

Bean, C., Lokmer, I., & O'Brien, G. (2008). Influence of near-surface volcanic structure on long-period seismic signals and on moment tensor inversions: Simulated examples from Mount Etna. *Journal of Geophysical Research*, *113*, B08308. https://doi.org/10.1029/2007jb005468

Beilecke, T., Krawczyk, C. M., Ziesch, J., & Tanner, D. C. (2016). Near-surface fault detection using high-resolution shear wave reflection seismics at the CO2CRC Otway Project site, Australia. *Journal of Geophysical Research: Solid Earth*, *121*, 6510–6532. https://doi.org/10.1002/2015jb012668

Berkhout, A. (1981). Wave field extrapolation techniques in seismic migration, a tutorial. *Geophysics*, *46*(12), 1638–1656.

Berryhill, J. R. (1979). Wave-equation datuming. *Geophysics*, *44*(8), 1329–1344.

Bevc, D. (1997). Flooding the topography: Wave-equation datuming of land data with rugged acquisition topography. *Geophysics*, *62*(5), 1558–1569.

Bharadwaj, P., Schuster, G., Mallinson, I., & Dai, W. (2012). Theory of supervirtual refraction interferometry. *Geophysical Journal International*, *188*(1), 263–273.

Claerbout, J., & Fomel, S. (2006). Image estimation by example: Geophysical soundings image construction. Stanford Exploration Project.

Curtis, A., & Halliday, D. (2010). Source-receiver wave field interferometry. *Physical Review E*, *81*(4), 046601.

Dong, S., Luo, Y., Xiao, X., Chávez-Pérez, S., & Schuster, G. T. (2009). Fast 3D target-oriented reverse-time datuming. *Geophysics*, *74*(6), WCA141–WCA151.

Everett, M. E. (2012). Theoretical developments in electromagnetic induction geophysics with selected applications in the near surface. *Surveys in Geophysics*, *33*(1), 29–63.

Everett, M. E. (2013). *Near-surface applied geophysics*. Cambridge: Cambridge University Press.

Fehmers, G. C., & Höcker, C. F. W. (2003). Fast structural interpretation with structure-oriented filtering. *Geophysics*, *68*(4), 1286–1293.

Fomel, S. (2002). Applications of plane-wave destruction filters. *Geophysics*, *67*(6), 1946–1960. https://doi.org/10.1190/1.1527095

Fomel, S. (2010). Predictive painting of 3D seismic volumes. *Geophysics*, *75*(4), A25–A30.

Göğüş, O. H., & Pysklywec, R. N. (2008). Near-surface diagnostics of dripping or delaminating lithosphere. *Journal of Geophysical Research*, *113*, B11404. https://doi.org/10.1029/2007jb005123

Halliday, D., & Curtis, A. (2010). An interferometric theory of source-receiver scattering and imaging. *Geophysics*, *75*(6), SA95–SA103.

Hestenes, M. R., & Stiefel, E. (1952). Methods of conjugate gradients for solving linear systems, NBS Washington, DC.

Keho, T. H., & Kelamis, P. G. (2012). Focus on land seismic technology: The near-surface challenge. *The Leading Edge*, *31*(1), 62–68.

Kelamis, P. G., Erickson, K. E., Verschuur, D. J., & Berkhout, A. J. (2002). Velocity-independent redatuming: A new approach to the near-surface problem in land seismic data processing. *The Leading Edge*, *21*(8), 730–735.

Korneev, V., & Bakulin, A. (2006). On the fundamentals of the virtual source method. *Geophysics*, *71*(3), A13–A17.

Kragh, E., & Christie, P. (2002). Seismic repeatability, normalized rms, and predictability. *The Leading Edge*, *21*(7), 640–647. https://doi.org/10.1190/1.1497316

Mallinson, I., Bharadwaj, P., Schuster, G., & Jakubowicz, H. (2011). Enhanced refractor imaging by supervirtual interferometry. *The Leading Edge*, *30*(5), 546–550.

Marfurt, K. J. (2006). Robust estimates of 3D reflector dip and azimuth. *Geophysics*, *71*(4), 29–P40.

Nakata, N., & Snieder, R. (2012). Estimating near-surface shear wave velocities in Japan by applying seismic interferometry to KiK-net data. *Journal of Geophysical Research*, *117*, B01308. https://doi.org/10.1029/2011JB008595

Ramírez, A. C., & Weglein, A. B. (2009). Green's theorem as a comprehensive framework for data reconstruction, regularization, wavefield separation, seismic interferometry, and wavelet estimation: A tutorial. *Geophysics*, *74*(6), W35–W62.

Rickett, J., & Claerbout, J. (1999). Acoustic daylight imaging via spectral factorization: Helioseismology and reservoir monitoring. *The Leading Edge*, *18*(8), 957–960.

Ronen, J. (1987). Wave-equation trace interpolation. *Geophysics*, *52*(7), 973–984.

Schneider, W. A. Jr., Phillip, L. D., & Paal, E. F. (1995). Wave-equation velocity replacement of the low-velocity layer for overthrust-belt data. *Geophysics*, *60*(2), 573–579.

Schuster, G. T., Yu, J., Sheng, J., & Rickett, J. (2004). Interferometric/daylight seismic imaging. *Geophysical Journal International*, *157*(2), 838–852. https://doi.org/10.1111/j.1365-246X.2004.02251.x

Schuster, G. T., & Zhou, M. (2006). A theoretical overview of model-based and correlation-based redatuming methods. *Geophysics*, *71*, SI103–SI110.

Snieder, R., Grêt, A., Douma, H., & Scales, J. (2002). Coda wave interferometry for estimating nonlinear behavior in seismic velocity. *Science*, *295*(5563), 2253–2255.

Spitz, S. (1991). Seismic trace interpolation in the FX domain. *Geophysics*, *56*(6), 785–794.

Van Der Neut, J., Alexandrov, D., & Bakulin, A. (2015). Shallow virtual source redatuming by multi-dimensional deconvolution. *Geophysical Prospecting*, *64*(1), 4–18.

Wapenaar, K. (2004). Retrieving the elastodynamic Green's function of an arbitrary inhomogeneous medium by cross correlation. *Physical Review Letters*, *93*(25), 254301.

Wapenaar, K., Van Der Neut, J., Ruigrok, E., Draganov, D., Hunziker, J., Slob, E., et al. (2011). Seismic interferometry by crosscorrelation and by multidimensional deconvolution: A systematic comparison. *Geophysical Journal International*, *185*(3), 1335–1364.

Weemstra, C., Westra, W., Snieder, R., & Boschi, L. (2014). On estimating attenuation from the amplitude of the spectrally whitened ambient seismic field. *Geophysical Journal International*, *197*(3), 1770–1788.

Xue, Z., Zhang, H., Zhao, Y., & Fomel, S. (2019). Pattern-guided dip estimation with plane-wave destruction filters. *Geophysical Prospecting*, *67*(7), 1798–1810. https://doi.org/10.1111/1365-2478.12798

Yilmaz, Ö. (2001), Seismic data analysis: Processing, inversion, and interpretation of seismic data, Society of Exploration Geophysicists.

Zhang, H., Thurber, C., & Rowe, C. (2003). Automatic P-wave arrival detection and picking with multiscale wavelet analysis for single-component recordings. *Bulletin of the Seismological Society of America*, *93*(5), 1904–1912.

Zhao, Y., & Li, W. (2018a). Model-based radiation pattern correction for interferometric redatuming in 4D seismic. *Geophysics*, *83*(4), Q25–Q35.

Zhao, Y., & Li, W. (2018b). Wavelet-crosscorrelation-based interferometric redatuming in 4D seismic. *Geophysics*, *83*(4), Q37–Q47.

Zhao, Y., Liu, T., Tang, G., Zhang, H., & Sengupta, M. (2019). Virtual-source imaging and repeatability for complex near surface. *Scientific Reports*, *9*(1), 1–18.

Zhao, Y., Zhang, H., Liu, H., Zhang, D., & Sengupta, M. (2018). Target-oriented diversity stacking for virtual-source imaging and monitoring. *The Leading Edge*, *37*(10), 764–773.